Part Four
Photoinduced Modification of Materials and Femtochemistry

17
Theory of Femtochemistry at Metal Surfaces: Associative Molecular Photodesorption as a Case Study

Peter Saalfrank, Tillmann Klamroth, Tijo Vazhappilly, and Rigoberto Hernandez

17.1
Introduction

Reactions on surfaces are of great scientific interest because of their diverse applications. Well-known examples are the production of ammonia on metal surfaces for fertilizers and reduction of poisonous gases from automobiles using catalytic converters [1]. For these applications, metal surfaces – most notably, those consisting of transition metals – are particularly interesting as they offer a great variety of electronic structure and, therefore, "tunability" toward specific targets.

Photoinduced reactions at surfaces were also studied in detail [2–5]. These are useful, for example, for photocatalysis and nanostructuring of surfaces. Some of these reactions are occurring on femtosecond ($1\,\mathrm{fs} = 10^{-15}\,\mathrm{s}$) timescale [6]. The advent of femtosecond lasers – that is, ultrashort and intense laser pulses – offers the possibility to monitor these motions in real time, for example, by two-pulse correlation techniques. Moreover, femtochemistry at metal surfaces can be very distinct – on quantitative and qualitative scales – from more traditional surface photochemistry driven by conventional light sources [5, 6].

Photochemistry at metal surfaces may or may not proceed *indirectly*, that is, by initial excitation of the substrate electrons rather than by direct excitation of the adsorbate. One way to distinguish between the direct or the substrate-mediated route is through a dependence (direct) [7], or lack thereof (substrate mediated) [8, 9], of the reaction cross section on the polarization of the incoming light. In particular for initiating photons in the UV/vis regime, which can deeply penetrate into metal surfaces [10], indirect mechanisms have been suggested to be operative in many cases. Further, when femtosecond lasers (FLs) are used, hot metal electrons that are attached to the adsorbate are believed to often trigger the reaction rather than phonons [6, 11] (see below). For the reaction of interest below, photodesorption of H_2 from Ru(0001), experiments suggest a substrate-mediated, hot-electron-driven mechanism [12].

The indirect, substrate-mediated excitation can also be categorized according to its fluence dependence. For the prototypical case of photodesorption, for example,

low-fluence, nanosecond lasers enforce so-called DIET, desorption induced by electronic transitions, for which the desorption probability Y scales *linearly* with laser fluence [2–5]. DIET is a result of infrequent and uncorrelated electronic excitations of the adsorbate–substrate complex. In the desorption of adsorbates from metals, the excited state is often a *negative ion resonance* formed by electron attachment of excited electrons in the substrate to the adsorbate. The resonance is short-lived with an electronic lifetime τ_{el} typically as short as femtoseconds [6]. Desorption occurs in the ground state after electronic quenching on this timescale. The adsorbate also relaxes vibrationally, by vibration-electron coupling, with a vibrational lifetime τ_{vib} typically in the order of picoseconds [13]. DIET occurs if the average time between two subsequent electronic excitations, t_{exc}, is long as compared to these lifetimes.

In contrast, in the presence of intense femtosecond laser pulses, one observes so-called DIMET, desorption induced by multiple electronic transitions [14–17]. The short, but intense, laser pulses can cause more than one photon collision with the substrate during the course of an event leading to multiple excitations of the adsorbate on the timescales of electronic and vibrational relaxation. The pulse creates "hot electrons" in the metal surface, which enforce "ladder climbing" of the adsorbate on the electronic ground state into the desorption continuum. The FL pulse may also heat surface and bulk phonons, thus leading to thermal desorption. Experimentally, one can discriminate between phonon and electronic mechanisms by two-pulse correlation (2PC) traces [16]. Accordingly, one records observables such as the desorption yield Y, as a function of the delay time $\Delta\tau$ between two laser pulses: Correlations on ultrashort timescales (approximately picoseconds [6]) are indicative of an electronic mechanism.

A "hallmark" of DIMET is its *superlinear* increase of the desorption yield with laser fluence, F, frequently fitted as a power law

$$Y = A \, F^n \tag{17.1}$$

with $n > 1$ (typically 2–10). An example – see below – is associative desorption of H_2 from Ru(0001) by FL pulses, where $n \approx 3$ has been observed experimentally [12, 18, 19]. A second key difference between DIMET and DIET is that DIMET typically leads to higher yields but – due to electronic quenching – they are still low as compared to yields for photoreactions at insulators. A third "hallmark" of DIMET is that also its energy distribution into various degrees of freedom of the desorbing particles is fluence dependent. For example, for 2D:Ru(0001), the translational energy of desorbing D_2 changes from about 300–500 meV in the fluence range $F \in \{60, 120\}$ J/m^2 according to experiment [19]. In general, photoreactions such as DIET and DIMET can show a nonequal and nonthermal energy distribution into various degrees of freedom. For DIMET of H_2 from Ru(0001), for example, translation is typically "hotter" than vibration by a factor of about 4 [19]. The precise value depends on the laser fluence.

This chapter focuses on a comparison of various methods and models to treat FL-induced photochemistry at metal surfaces theoretically. In particular, we will consider DIMET of H_2 and D_2 from Ru(0001), which has been studied experimentally in

Refs [12, 18, 19], and theoretically in Refs [20] and [21, 22]. While our analysis is presented only for a specific system and reaction, it is expected to be relevant also for other FL-induced reactions at metal surfaces [23].

17.2
Theory of Femtochemistry at Surfaces

In this section, several theoretical models to rationalize femtochemistry at surfaces will be reviewed. We will distinguish, somewhat arbitrarily, between "weakly non-adiabatic" and "strongly nonadiabatic" models. We further distinguish classical (or quasiclassical) approaches in which the nuclear motion is described by classical mechanics from quantum dynamical approaches that account properly for quantum mechanical effects such as zero-point motion and tunneling.

17.2.1
Weakly Nonadiabatic Models

We use the term "weakly nonadiabatic" in cases when the dynamics is dominated by nuclear motion on a single (ground-state) potential energy surface, with electronic transitions to excited states serving merely to drive the dynamics on the ground state. Besides many hot-electron-driven reactions, a further physical example of this type is the vibrational relaxation of adsorbates at metal surfaces by vibration-electron coupling [13].

17.2.1.1 Two- and Three-Temperature Models
Hot-electron-mediated femtochemistry at metals can be treated by two- or three-temperature models in conjunction with classical Langevin dynamics, master equation approaches, or with Arrhenius-type rate equations. All of these are based on the concept of "electronic friction," and the assumption that temperatures can be assigned to various subsystems (electrons, phonons, and adsorbate vibrations) of the adsorbate–substrate complex. Accordingly, in a typical experiment, the laser pulse is absorbed by the metal thereby heating the electrons to a time-dependent (and generally also coordinate-dependent) electron temperature, $T_{el}(t)$. By electron–phonon coupling, phonons are also excited giving rise to a phonon temperature $T_{ph}(t)$. This can be described by the two-temperature model (2TM), where one solves two coupled equations [24, 25]

$$C_{el} \frac{\partial T_{el}}{\partial t} = \frac{\partial}{\partial z} \varkappa \frac{\partial}{\partial z} T_{el} - g(T_{el} - T_{ph}) + S(z, t) \tag{17.2}$$

$$C_{ph} \frac{\partial T_{ph}}{\partial t} = g(T_{el} - T_{ph}) \tag{17.3}$$

for the electron and phonon temperatures T_{el} and T_{ph} within the metal. In Eqs. (17.2) and (17.3), C_{el} and C_{ph} are electron and lattice specific heat constants, respectively,

which can be calculated from the electron specific heat constant, the Debye temperature, and the density of the solid. According to Eq. (17.2), $T_{el}(t)$ is affected by thermal diffusion along a coordinate z in direction perpendicular to the surface, as indicated in the first term on the rhs. Here, $\varkappa = \varkappa_0 \, T_{el}/T_{ph}$ is the thermal conductivity and $\varkappa_0$ an empirical parameter. $T_{el}(t)$ is also affected by electron–phonon coupling (second term, with g = electron–phonon coupling constant), and the external laser pulse that gives rise to a time- and coordinate-dependent source term (third term). Assuming a laser pulse of Gaussian temporal shape, the source term is given by

$$S(z,t) = \frac{F e^{-\frac{z}{\zeta}}}{\zeta} \frac{e^{-\frac{t^2}{2\sigma^2}}}{\sqrt{2\pi}\sigma}. \tag{17.4}$$

Here, ζ is the optical penetration depth calculated from $\zeta = \frac{\lambda}{4\pi n_I}$, where λ is the wavelength of the femtosecond laser and n_I the imaginary part of the refractive index. Further, σ is the width parameter for the Gaussian. For a Gaussian pulse, the fluence is $F = E_0^2 \varepsilon_0 c \sigma \frac{\sqrt{\pi}}{2}$, where E_0 is the field amplitude, ε_0 the vacuum permittivity, and c the speed of light. In summary, for the calculation of T_{el} and T_{ph} in the 2TM a set of internal (material) and external (laser) parameters is required.

As an example, we show results of the 2TM for a Ru surface in Figure 17.1a, when excited by various femtosecond laser pulses to be used for modeling DIMET of H_2
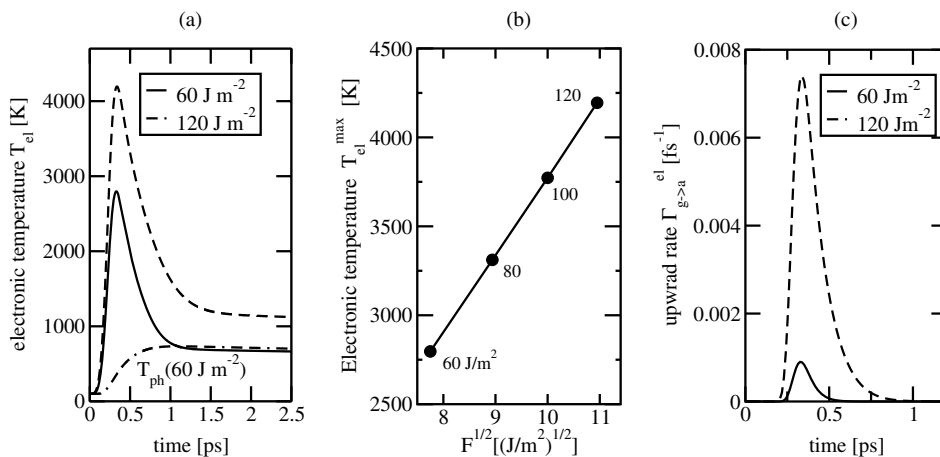
Figure 17.1 (a) Electronic temperatures calculated for Ru from the 2TM with two different laser fluences. The dashed-dotted curve represents the phonon temperature, T_{ph}, for a fluence of 60 J/m². Gaussian pulse parameters: FWHM $= \sqrt{8\ln 2}\,\sigma = 130$ fs, $\lambda = 800$ nm. The material parameters entering the 2TM are Electron–phonon coupling constant, $g = 185 \times 10^{16}$ W/m³/K; electron specific heat constant, $\gamma = 400$ J/m³/K²; thermal conductivity, $\varkappa_0 = 117$ W/m/K; Debye temperature, $\theta = 600$ K; density, $\varrho_0 = 12370$ kg/m³; optical penetration depth at $\lambda = 800$ nm, $\varsigma = 15.6$ nm. (b) Maximum electronic temperature T_{el}^{max} calculated from the 2TM, plotted as a function of the square root of laser fluence, $\sqrt{F}$, showing an approximate relation $T_{el}^{max} \propto \sqrt{F}$. (c) Dependence of the upward rate $\Gamma_{g \to a}^{el}$ for 2H:Ru(0001) on the applied laser fluence calculated from Eq. (17.20). Parameters: $\Gamma_{a \to g}^{el} = (2 \text{ fs})^{-1}$, $\Delta V = 1.55$ eV.

from Ru(0001). The 2TM predicts a maximum electronic temperature of several thousand Kelvin around a few hundred femtosecond, before equilibration with the lattice occurs. The maximum electronic temperature increases with increasing fluence roughly according to $T_{el}^{max} \propto \sqrt{F}$ as indicated in Figure 17.1b, in agreement with earlier findings [26, 27]. Thus, the laser fluence can be used as a control parameter to enhance reaction yields. Another efficient control parameter that also affects T_{el}^{max} is the thickness d of a metal film, if films are used rather than bulk metals [10, 27].

17.2.1.2 One-Dimensional Classical, Arrhenius-Type Models

In the simplest theoretical models of FL-induced photodesorption, the 2TM is often extended to a three-temperature model (3TM). Here, one also assigns a temperature $T_{ads}(t)$ to the adsorbate-surface vibration (or to an internal mode), which arises from the coupling of this mode to the electrons or phonons of the metal. This can be described by an *electron-vibration coupling constant*, η_{el}, and a *vibration-phonon coupling constant*, η_{ph}, respectively. Often the electronic channel dominates. If the concept of thermal equilibration of the active adsorbate is accepted, it can be shown [28] from a Langevin model for the electron heat bath that

$$\frac{\partial T_{ads}}{\partial t} = \eta_{el} \left(T_{el} - T_{ads} \right). \tag{17.5}$$

Equation (17.5) must be solved in addition to Eqs. (17.2) and (17.3), resulting in the 3TM. The basic concepts of the 3TM are illustrated in Figure 17.2a.

Given $T_{ads}(t)$, in a classical, one-dimensional limit [28] where the reaction proceeds along a reaction coordinate, q (e.g., the adsorbate–surface distance), the desorption rate is given as

$$R_{des} = \frac{D \, \eta_{el}}{k_B \, T_{ads}(t)} \exp\left\{ -\frac{D}{k_B \, T_{ads}(t)} \right\}. \tag{17.6}$$

Here, k_B is Boltzmann's constant, and D an activation energy that can be interpreted, formally, as the adsorption energy of the molecule (see Figure 17.2b). In practice, D and η_{el} are frequently used as model parameters to fit experimental data. Related Arrhenius-type expressions have been suggested elsewhere [16, 17].
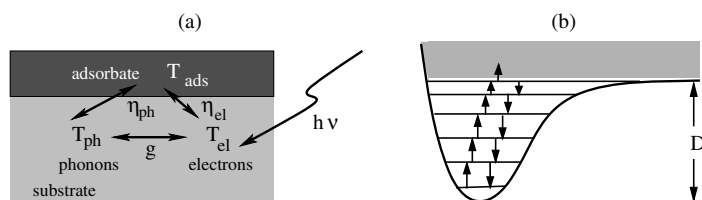
Figure 17.2 (a) Illustration of the three-temperature model, see text. (b) Illustration of a substrate-mediated, photochemical "ladder climbing" process into the continuum of a ground-state potential. Alternatively, Arrhenius-type expressions such as Eq. (17.6) describe the desorption process, with D playing the role of an activation energy (see text). Adapted in part with permission from [23]. Copyright 2006 American Chemical Society.

Arrhenius models are limited to one-dimensional reaction coordinates, treat nuclear motion classically, and assume the existence of electronic and vibrational temperatures even though the conditions are not at equilibrium. The concept of a thermal electron bath is questionable at least within the first few 100 fs or so, after the pulse, according to experimental [29] and theoretical evidence [30, 31]. The concept of an adsorbate temperature can be inaccurate for even much longer timescales [32, 33].

17.2.1.3 Langevin Dynamics with Electronic Friction

Some of the restrictions discussed above can be overcome by Langevin molecular dynamics with electronic friction [34]. Here, nuclear motion is still classical, and the electronic degrees of freedom are expressed in the form of a friction and fluctuating forces. If q is the only degree of freedom considered (e.g., the molecule-surface distance Z with associated reduced mass, m_q), the equation of motion is

$$m_q \frac{d^2 q}{dt^2} = -\frac{dV}{dq} - \eta_{qq} \frac{dq}{dt} + R_q(t). \tag{17.7}$$

Here, V is the ground state potential, and η_{qq} is related to the electronic friction coefficient of above through $\eta_{qq} = m_q \eta_{el}$. $R_q(t)$ is a fluctuating force that obeys a fluctuation–dissipation theorem, and depends on the electronic temperature, $T_{el}(t)$, obtained from the 2TM. When modeled as Gaussian white noise, the random force has the properties

$$\langle R_q(t) \rangle = 0 \tag{17.8}$$

$$\langle R_q(t) | R_q(t') \rangle = 2 k_B T_{el} \eta_{qq} \, \delta(t-t'). \tag{17.9}$$

$R(t)$ can be calculated from the Box–Müller algorithm [35] as

$$R_q(t) = \left[\frac{2 k_B T_{el}(t) \eta_{qq}}{\Delta t} \right]^{\frac{1}{2}} (-2\ln b)^{\frac{1}{2}} \cos 2\pi c \tag{17.10}$$

where Δt is the time step, and b and c are random numbers uniformly distributed on the interval [0,1]. This equation shows clearly that if the electronic temperature is zero, or if electronic friction vanishes, we have no random force. Increasing the electronic temperature at finite friction, on the other hand (e.g., by a laser pulse according to the 2TM), leads to large random forces that may drive a photoreaction.

Various methods, based, for example, on Hartree–Fock cluster calculations [34] or on periodic density functional theory (DFT) [36], have been suggested to calculate the friction coefficient from first principles. All of these methods are based on a perturbative, golden rule-type treatment of the vibration-electron coupling. For example, the diagonal electronic friction coefficients are determined from (periodic) DFT as

$$\eta_{qq} = 2\pi\hbar \sum_{\alpha,\beta} \left| \left\langle \psi_\alpha \left| \frac{\delta \nu}{\delta q} \right| \psi_\beta \right\rangle \right|^2 \delta(\varepsilon_\alpha - \varepsilon_F) \, \delta(\varepsilon_\beta - \varepsilon_F), \tag{17.11}$$

where $\psi_{\alpha(\beta)}$ and $\varepsilon_{\alpha(\beta)}$ are Kohn–Sham orbitals and energies for combined band and k-point index $\alpha(\beta)$. Further, ε_F is the Fermi energy and $\frac{\delta v}{\delta q}$ the functional derivative of the exchange–correlation functional with respect to nuclear coordinate q. The electronic friction coefficient is also directly related to the vibrational relaxation rate, and thus to the vibrational lifetime τ_{vib}. At zero temperature, the vibrational relaxation rate $\Gamma^{vib}_{1 \to 0}$ of the first excited vibrational level of the mode of interest is simply

$$\Gamma^{vib}_{1 \to 0} = \tau^{-1}_{vib} = \eta_{el}. \tag{17.12}$$

Equation (17.7) can be easily generalized to more degrees of freedom by interpreting the friction coefficient as a tensor with elements $\eta_{qq'}$ [34, 36] and extending the equation of motion (17.7) by a coupling term $-\sum_{q' \neq q} \eta_{qq'} \frac{dq'}{dt}$. In general, there are F^2 tensor matrix elements $\eta_{qq'}$ each of which depends on F degrees of freedom $q_1, \ldots, q_F$ for an F-dimensional system. This can be extremely demanding computationally, which is why one often neglects off-diagonal elements $\eta_{qq'}$ for $q \neq q'$ and/or makes additional approximations regarding the coordinate dependence of η_{qq} [36].

17.2.1.4 Quantum Treatment with Master Equations

The Langevin approach is multidimensional and free of the assumption of vibrational temperatures, but still classical. The classical approximation can be overcome with the help of master equations,

$$\frac{dP_\alpha}{dt} = \sum_\beta W_{\beta \to \alpha} P_\beta(t) - \sum_\beta W_{\alpha \to \beta} P_\alpha(t), \tag{17.13}$$

giving the population P_α of state $|\alpha\rangle$ of the ground state potential. The latter can be derived from (multidimensional) system Hamiltonians. The populations are determined by interlevel transition rates,

$$W_{\alpha \to \beta} = \Gamma^{vib}_{\alpha \to \beta} + W^{ex}_{\alpha \to \beta}. \tag{17.14}$$

Here, $\Gamma^{vib}_{\alpha \to \beta}$ is a vibrational relaxation rate or re-excitation rate if the temperature is finite. $W^{ex}_{\alpha \to \beta}$ is a rate caused by an external energy source that drives the "ladder climbing." For example, for FL-induced, hot-electron-mediated reactions driven by electron attachment to form a negative ion resonance, the transition rates calculated perturbatively depend on the electron temperature $T_{el}(t)$, and the energetic position ε_a and width Δ_a of the adsorbate resonance as shown elsewhere [33, 37].

By solving Eq. (17.13), a reaction probability can be defined by analyzing those populations that reach the desorption continuum, with an energy $E_\alpha > D$ where D is again the binding energy of the adsorbate if "desorption" is the reaction of interest. Such a damped ladder climbing process is schematically illustrated in Figure 17.2b. As a simplification, in the so-called "truncated harmonic oscillator" (THO) model and when additionally assuming that the P_α is a Boltzmann distribution associated with a vibrational temperature T_{ads}, the master equation (17.13) simplifies to reaction rates R of the Arrhenius type as in Eq. (17.6) [37].

17.2.2
Strongly Nonadiabatic Dynamics

In contrast to weakly nonadiabatic dynamics, "strongly nonadiabatic" dynamics requires the explicit inclusion of electronically excited states. Examples where this is necessary are resonant charge transfer during atom-surface scattering and reactions proceeding through long-lived excited states, such as adsorbate excitations at insulators. Of course, any photoreaction at a metal surface with short-lived excited states can also be described in this way.

17.2.2.1 Multistate Time-Dependent Schrödinger Equation

The most general approach to treating nonadiabatic dynamics is by a coupled, multistate time-dependent Schrödinger equation (TDSE). As the initial condition, we assume that the system is initially in a product of its electronic ground state $|g\rangle$ and an arbitrary nuclear wave function $\psi_g(R, t)$ (where R denotes a set of nuclear coordinates). Assuming that only a single, excited adsorbate state $|a\rangle$ is of importance, the TDSE reads

$$
i\hbar \frac{\partial}{\partial t}
\begin{pmatrix}
\psi_a \\
\psi_g \\
\psi_{k_1} \\
\psi_{k_2} \\
\vdots
\end{pmatrix}
=
\begin{pmatrix}
\hat{H}_a & V_{ag} & V_{ak_1} & V_{ak_2} & & \cdots \\
V_{ga} & \hat{H}_g & V_{gk_1} & V_{gk_2} & & \cdots \\
V_{k_1a} & V_{k_1g} & \hat{H}_{k_1} & V_{k_1k_2} & V_{k_1k_3} & \cdots \\
V_{k_2a} & V_{k_2g} & V_{k_2k_1} & \hat{H}_{k_2} & V_{k_2k_1} & \cdots \\
\vdots & \vdots & \vdots & \vdots & \vdots & \ddots
\end{pmatrix}
\begin{pmatrix}
\psi_a \\
\psi_g \\
\psi_{k_1} \\
\psi_{k_2} \\
\vdots
\end{pmatrix}.
\qquad (17.15)
$$

In Eq. (17.15), a discretized continuum of substrate-excited states $|k_i\rangle$ was included to model a metal surface. The diagonal elements of the Hamiltonian matrix are $\hat{H}_n = \hat{T}_{\text{nuc}} + V_n(R)$ with $\hat{T}_{\text{nuc}}$ being the nuclear kinetic energy operator, and $V_n(R)$ the potential energy curve for state $|n\rangle$. The off-diagonal elements $V_{nm}(R, t)$ stand for general couplings between different electronic states, for example, for direct dipole, spin-orbit, or non-Born–Oppenheimer couplings, the latter expressed here as potential couplings in a diabatic representation. The multistate model is illustrated schematically in Figure 17.3a. Equation (17.15) can hardly ever be solved in practice. In particular, for metals with a continuum of electronic excitations, the basis of the latter is often far too large to be computationally tractable.

17.2.2.2 Open-System Density Matrix Theory

An alternative is to map the closed-system, *N*-state model (17.15) on an open-system, *reduced* density matrix model with only a few relevant states. In particular, two-state models are common, and retain only the ground $|g\rangle$ and excited $|a\rangle$ states. Here, the excited state (e.g., the negative ion state) is treated as a nonstationary *resonance* with a finite energetic width Δ_a. The energy is generally not conserved in contrast to the unitary approach using the TDSE – see Figure 17.3b for illustration. The resonance width, Δ_a, can in principle be calculated from the non-Born–Oppenheimer coupling
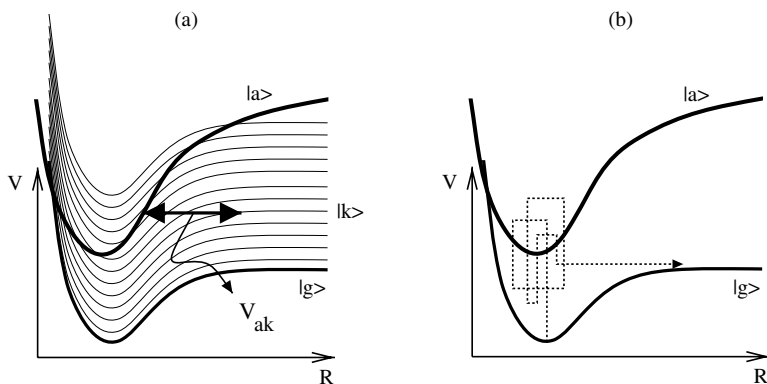
Figure 17.3 (a) The coherent, coupled multistate model of a nonadiabatic surface process, with ground state $|g\rangle$, a photoactive excited state $|a\rangle$, and a (quasi-) continuum of substrate-excited states $|k\rangle$. A non-Born–Oppenheimer coupling element V_{ak} is indicated. (b) Illustration of the corresponding open-system two-state model, realized with the MCWP approach or its classical variant. The dashed curve indicates a (quantum) trajectory schematically, with multiple transitions between the ground state $|g\rangle$ and resonance state $|a\rangle$. The latter has a finite energetic width, $\Delta_a = \hbar\Gamma^{el}_{a\rightarrow g}$. Adapted in part with permission from [23]. Copyright 2006 American Chemical Society.

matrix elements V_{ak} that couple metal continuum states $|k\rangle$ to the excited state $|a\rangle$, using, for instance, a Newns–Anderson approach [38, 39]. Often, the resonance width is treated as an empirical parameter instead. In general, the resonance width Δ_a depends on the nuclear coordinates R. If this dependence is neglected, the resonance decays strictly exponentially with an ultrashort (approximately femtoseconds) electronic lifetime

$$\tau_{el} = \frac{\hbar}{\Delta_a} = 1/\Gamma^{el}_{a\rightarrow g}, \tag{17.16}$$

Here, $\Gamma^{el}_{a\rightarrow g}$ is the electronic quenching rate.

The suggested equation of motion for the open-system two-state model of DIMET has been cast in the form of a Liouville–von Neumann (LvN) equation [40, 41]

$$\frac{\partial}{\partial t}\begin{pmatrix} \hat{\varrho}_a & \hat{\varrho}_{ag} \\ \hat{\varrho}_{ga} & \hat{\varrho}_g \end{pmatrix} = -\frac{i}{\hbar}\left[\begin{pmatrix} \hat{H}_a & V_{ag} \\ V_{ga} & \hat{H}_g \end{pmatrix}, \begin{pmatrix} \hat{\varrho}_a & \hat{\varrho}_{ag} \\ \hat{\varrho}_{ga} & \hat{\varrho}_g \end{pmatrix} \right]$$
$$+ \frac{\partial}{\partial t}\begin{pmatrix} \hat{\varrho}_a & \hat{\varrho}_{ag} \\ \hat{\varrho}_{ga} & \hat{\varrho}_g \end{pmatrix}_{rel} + \frac{\partial}{\partial t}\begin{pmatrix} \hat{\varrho}_a & \hat{\varrho}_{ag} \\ \hat{\varrho}_{ga} & \hat{\varrho}_g \end{pmatrix}_{exc}. \tag{17.17}$$

In Eq. (17.17), $\hat{\varrho}_i$ and $\hat{\varrho}_{ij}$ are the diagonal and off-diagonal reduced density operators in the vibrational space of the ground and excited states.

The first term on the rhs of Eq. (17.17) describes the coherent evolution of the system, with possible direct couplings. In Eq. (17.17), "rel" accounts for energy relaxation of the resonance state $|a\rangle$ with an electronic relaxation rate $\Gamma^{el}_{a\rightarrow g}$ according to

$$\frac{\partial}{\partial t}\begin{pmatrix}\hat{\varrho}_a & \hat{\varrho}_{ag} \\ \hat{\varrho}_{ga} & \hat{\varrho}_g\end{pmatrix}_{\text{rel}} = \Gamma^{\text{el}}_{a\to g}\begin{pmatrix} -\hat{\varrho}_a & -\dfrac{\hat{\varrho}_{ag}}{2} \\[2mm] -\dfrac{\hat{\varrho}_{ga}}{2} & +\hat{\varrho}_a \end{pmatrix} \tag{17.18}$$

and "exc" describes the hot-electron-, substrate-mediated excitation of the adsorbate–substrate complex [40, 41], which depopulates the ground state:

$$\frac{\partial}{\partial t}\begin{pmatrix}\hat{\varrho}_a & \hat{\varrho}_{ag} \\ \hat{\varrho}_{ga} & \hat{\varrho}_g\end{pmatrix}_{\text{exc}} = \Gamma^{\text{el}}_{g\to a}(t)\begin{pmatrix} +\hat{\varrho}_g & -\dfrac{\hat{\varrho}_{ag}}{2} \\[2mm] -\dfrac{\hat{\varrho}_{ga}}{2} & -\hat{\varrho}_g \end{pmatrix}. \tag{17.19}$$

For DIMET, the initial condition is $\hat{\varrho}_0 = |g\rangle\langle g| \otimes |\phi^g_0\rangle\langle\phi^g_0|$ if $T = 0$, that is, the system is in the ground vibrational state at the ground-state surface. Further,

$$\Gamma^{\text{el}}_{g\to a}(t) = \Gamma^{\text{el}}_{a\to g}\exp\left\{-\frac{V_a - V_g}{k_{\text{B}}\,T_{\text{el}}(t)}\right\} \tag{17.20}$$

is a time-dependent upward rate that obeys detailed balance. The assumption of an electronic temperature, which can be calculated from the 2TM, is also made in Eq. (17.20). Since both the excited- and ground-state potentials V_a and V_g depend on all nuclear coordinates, $\Gamma^{\text{el}}_{g\to a}(t)$ is generally also coordinate-dependent, even for coordinate-independent quenching. Frequently, the approximation is made of $V_a - V_g$ being a constant, given by the potential difference at the Franck–Condon point that is assumed to coincide with the energy of the exciting laser. For 2H:Ru (0001), for example, the energy difference is 1.55 eV, corresponding to the excitation wavelength of 800 nm. For this system, the upward rates for laser fluences and $T_{\text{el}}(t)$ curves of Figure 17.1a are indicated in Figure 17.1c, where an excited-state lifetime of $\tau_{\text{el}} = 2$ fs has been assumed.

In passing we note that the two-state DIMET model of above can be recast in more compact notation as

$$\frac{\partial\hat{\varrho}_s}{\partial t} = -\frac{i}{\hbar}\left[\hat{H}_s, \hat{\varrho}_s\right] + \sum_{k=1}^{2}\left(\hat{C}_k\hat{\varrho}_s\hat{C}^{\dagger}_k - \frac{1}{2}\left[\hat{C}^{\dagger}_k\hat{C}_k, \hat{\varrho}_s\right]_+\right) \tag{17.21}$$

where $\hat{\varrho}_s = \hat{\varrho}_g|g\rangle\langle g| + \hat{\varrho}_a|a\rangle\langle a| + \hat{\varrho}_{ag}|a\rangle\langle g| + \hat{\varrho}_{ga}|g\rangle\langle a|$ is the system density operator and $\hat{H}_s = \hat{H}_g|g\rangle\langle g| + \hat{H}_a|a\rangle\langle a| + V_{ag}|a\rangle\langle g| + V_{ga}|g\rangle\langle a|$ is the system Hamiltonian. Further,

$$\hat{C}_1 = \sqrt{\Gamma^{\text{el}}_{a\to g}}|g\rangle\langle a| \tag{17.22}$$

$$\hat{C}_2 = \sqrt{\Gamma^{\text{el}}_{g\to a}(t)}|a\rangle\langle g| \tag{17.23}$$

are the so-called Lindblad operators for the relaxation ($k = 1$) and excitation ($k = 2$) process, respectively. In Eq. (17.21), $[\,]_+$ refers to an anticommutator. It is easy to

extend the formalism to account for further "dissipation channels," excitations with more than one laser pulse, and finite initial temperature [32].

17.2.2.3 Stochastic Wave Packet Approaches

Open-system density matrix theory is a quantum approach that is quadratically more costly than wave packet methods since matrices, rather than state vectors have to be propagated forward in time. Thus, the direct numerical solution of Eq. (17.21) is limited to low-dimensional models in which only a few, often only one, system modes are included. An alternative to the direct solution is stochastic wave packet approaches [42–44], which are easily applicable to LvN equations of the Lindblad form such as Eq. (17.21). Here, a matrix propagation is replaced by a set of stochastically selected wave packet (state vector) propagations. Thus, though costly, higher-dimensional problems can be treated quantum mechanically.

In particular, we refer to the Monte Carlo wave packet (MCWP) method [45], which has also been adopted for photodesorption problems [46–49]. For concreteness, suppose that $T = 0$ K of an arbitrary number K of dissipative channels, the algorithm works as follows:

1) We start with an initial wave function $|\psi(0)\rangle$, typically the vibrational ground state on the ground-state surface at $T = 0$ K.
2) An auxiliary wave function is created at every time step as $|\psi'(t + \Delta t)\rangle = \exp\left(-i\hat{H}'_s \Delta t/\hbar\right)|\psi(t)\rangle$, by propagating $|\psi(t)\rangle$ under the influence of a non-hermitian Hamiltonian, $\hat{H}'_s$, given by

$$\hat{H}'_s = \hat{H}_s - \frac{i\hbar}{2}\sum_k^K \hat{C}_k^\dagger \hat{C}_k \tag{17.24}$$

where, $\hat{C}_k$ are the Lindblad operators from Eq. (17.21). Due to the non-Hermiticity of the Hamiltonian, $|\psi'(t + \Delta t)\rangle$ is not normalized. The loss of norm Δp in each time step is

$$\Delta p = 1 - \langle \psi'(t + \Delta t)|\psi'(t + \Delta t)\rangle. \tag{17.25}$$

3) In each time step, a random number ε is drawn from a uniform distribution between 0 and 1. If $\Delta p > \varepsilon$, a quantum jump occurs, and the new wave function is chosen among the different possibilities $\hat{C}_k|\psi(t)\rangle$ with a probability $p_k = \Delta p_k/\Delta p$. Here, $\Delta p_k = \Delta t\langle \psi(t)|\hat{C}_k^\dagger \hat{C}_k|\psi(t)\rangle \geq 0$ is the approximate loss in dissipative channel k up to first-order. The new wave function is then calculated in normalized form as

$$|\psi(t + \Delta t)\rangle = \frac{\hat{C}_k|\psi(t)\rangle}{\langle \psi(t)|\hat{C}_k^\dagger \hat{C}_k|\psi(t)\rangle^{\frac{1}{2}}}. \tag{17.26}$$

For $\Delta p \leq \varepsilon$, no quantum jump occurs and the new wave function $|\psi(t + \Delta t)\rangle$ is obtained by renormalizing $|\psi'(t + \Delta t)\rangle$ as

$$|\psi(t + \Delta t)\rangle = \frac{|\psi'(t + \Delta t)\rangle}{(1 - \Delta p)^{\frac{1}{2}}}. \tag{17.27}$$

4) This procedure is repeated N times, that is, there are N "quantum trajectories." For each realization n, the expectation value of an operator $\hat{A}$ is calculated as

$$A_n(t) = \langle \psi_n(t) | \hat{A} | \psi_n(t) \rangle \tag{17.28}$$

and final expectation values of an operator $\hat{A}$ are obtained by averaging over N trajectories:

$$\langle \hat{A} \rangle (t) = \frac{1}{N} \sum_n^N A_n(t). \tag{17.29}$$

When applied to DIMET, the algorithm specializes as follows. Initially, the wave packet is on the ground-state surface, $|g\rangle$. The term $-\frac{i\hbar}{2}\hat{C_2}^\dagger \hat{C_2} = -\frac{i\hbar}{2}\Gamma_{g \to a}^{\text{el}}(t)|g\rangle \langle g|$ acts as a negative imaginary potential on the ground-state potential, which leads to a loss of norm of $\Delta p = 1 - e^{-\Gamma_{g \to a}^{\text{el}} \Delta t} \leq 1$ during time interval Δt. If $\Delta p > \varepsilon$, the wave packet jumps as a whole to the excited state $|a\rangle$, where it propagates under the influence of V_a and an imaginary absorber, $-\frac{i\hbar}{2}\Gamma_{a \to g}^{\text{el}}|a\rangle \langle a|$. The wave packet jumps back to the ground state $|g\rangle$ as soon as $\Delta p > \varepsilon$, where Δp is now given as $\Delta p = 1 - e^{-\Gamma_{a \to \varepsilon}^{\text{el}} \Delta t}$. Once in the ground state again, the wave packet can be re-excited provided the upward rate $\Gamma_{g \to a}^{\text{el}}(t)$ is still large. As a consequence, *multiple excitations* and de-excitations are possible during the action of the femtosecond laser pulse. In fact, the algorithm allows one to quantify the notion of *multiple* in DIMET by simply counting the number of quantum jumps from $|g\rangle$ to $|a\rangle$ and vice versa [22]. Again, one has to average over a large ensemble of quantum trajectories to arrive at meaningful results. For illustration, the desorption dynamics within the two-state MCWP model is illustrated schematically for a single trajectory in Figure 17.3b.

17.2.2.4 Quantum–Classical Hopping Schemes

The MCWP method is a quantum approach, and thus computationally demanding. One may, however, replace the quantum trajectories by classical trajectories while using the same procedure as in MCWP, that is, with transition probabilities calculated from the quenching rate $\Gamma_{a \to g}^{\text{el}}$ (for the relaxation process) and the excitation rates $\Gamma_{g \to a}^{\text{el}}(t)$ (for the FL-induced excitation process). This idea has been followed in the early, one-dimensional models of DIMET of diatomic molecules from metal surfaces [15]. Since more than one potential surface is involved, the method is a mixed quantum–classical approach with dissipation. Because nuclear dynamics is treated classically, the method can easily be extended to multidimensions, provided the relevant excited state potential energy surface(s) is (are) known.

There is also a quantum–classical approach to solve the nondissipative, coupled multistate Schrödinger equation (17.15), namely, the surface hopping method of Tully and coworkers [50]. In the latter, at each instant of time, the nuclear dynamics is described by a classical trajectory in one electronic state only. Hops or *switches*, between different electronic states $|n\rangle$ and $|m\rangle$ occur due to nonadiabatic couplings V_{nm}. Many ways exist of how to realize the switches in practice [50–54], and Tully's fewest switching algorithm [50] is a very popular one. The method has also been applied for nonadiabatic dynamics at surfaces [55, 56].

17.3
Femtosecond-Laser Driven Desorption of H$_2$ and D$_2$ from Ru(0001)

17.3.1
Experimental Facts

Several of the concepts discussed above will now be illustrated with the specific example of associative desorption of H$_2$ and D$_2$, from H- or D-covered Ru(0001) surfaces. The reaction has been studied by Frischkorn *et al.* using femtosecond lasers [12, 18, 19]. Their key experimental observations are as follows:

- Using 120–130 fs laser pulses at a wavelength of 800 nm and with fluences ranging from 60 to 120 J/m^2, associative desorption of H$_2$ and D$_2$ from a fully (1 × 1) H- or D-covered Ru(0001) surface has been observed.
- The recombinative desorption shows a large isotope effect with a desorption probability for H$_2$ typically 3–10 times higher than that of D$_2$ depending on fluence.
- The desorbing molecules have high translational energy compared to their vibrational energy.
- The desorption probability increases nonlinearly with laser fluence. At the same time, the isotope effect in the desorption probabilities goes down and the energy partitioning into different degrees of freedom is also fluence dependent.
- Two-pulse correlation experiments suggest that the reaction is probably due to a hot-electron-mediated mechanism with a short response time of ∼1 ps.

17.3.2
Potentials, Electronic Lifetime, and Friction

For theoretical modeling, both Langevin molecular dynamics with electronic friction and the quantum Monte Carlo wave packet two-state model have been used effectively [22].

17.3.2.1 The Ground-State Potential and Vibrational Levels
In both models, the same ground-state potential was adopted. We used a modified version of the six-dimensional (6D) potential of Luppi *et al.* [57, 58] calculated by periodic DFT for two H atoms per cell corresponding to a (2 × 2) coverage of H on Ru (0001). The DACAPO code [59] was adopted, using a plane wave basis, a three-layer relaxed slab model, and the so-called RPBE exchange–correlation functional [60]. The potential was fitted to an analytic form using the corrugation reducing procedure (CRP) [61]. From the 6D potential, a two-dimensional (2D) reduced dimensionality minimal model was constructed in which only the two most important coordinates for associative desorption are included. These are the distance of the center of mass of the molecule from the surface, Z, and the internal vibrational coordinate (H−H distance) of the desorbing molecule, r. The other four degrees of freedom of a diatomic molecule relative to a rigid surface, namely, lateral coordinates X and Y and
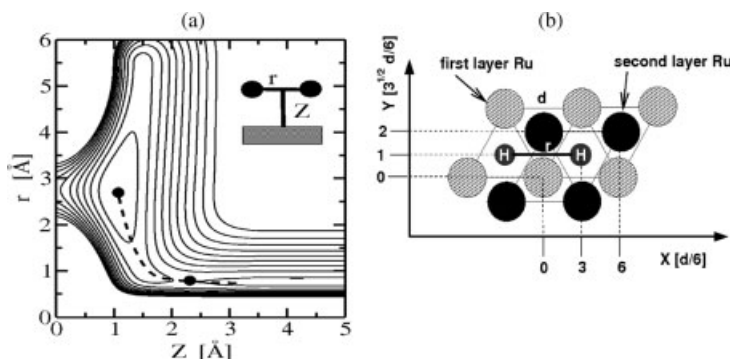
Figure 17.4 (a) Ground-state potential $V_g(r, Z)$ used in this work. Contours have an increment of 0.5 eV, starting at 0.5 eV. Bullets indicate the minimum at $Z_0 = 1.06$ Å and $r_0 = 2.75$ Å and the transition state at $Z^{\ddagger} = 2.24$ Å and $r^{\ddagger} = 0.77$ Å. The dotted line is the approximate minimum energy path S for the associative desorption. (b) Sketch of the coordinate system used. The H atoms reside in a plane defined by the interatomic axis, and the surface normal. Initially, they are in fcc (face-centered cubic) sites of the Ru(0001) surface. Adapted in part with permission from [22]. Copyright 2009 American Chemical Society.

azimuthal and polar angles φ and θ were fixed at their equilibrium values as $X_0 = 0$, $Y = \sqrt{3}d/6$, $\theta = 90°$, and $\varphi = 0°$. Here, $d = 2.75$ Å is the smallest distance between the two Ru atoms in the first layer of the Ru(0001) surface. These chosen coordinates are shown in Figure 17.4. The original potential was modified by extending it to regions that were not calculated in Ref. [62], and by adding smooth repulsive walls behind the transition states toward diffusion and subsurface adsorption. This allows one to model a full-coverage situation H-(1×1) as used in Ref. [12, 18], and to exclude subsurface adsorption after excitation [22].

The resultant two-dimensional PES, which is also shown in Figure 17.4(a), predicts an adsorption minimum at $Z_0 = 1.06$ Å and $r_0 = 2.75$ Å $(= d)$, with a binding energy of 0.85 eV (i.e., 0.42 eV per H atom). Further, in the 2D model, an incoming H_2 molecule feels a classical barrier of 0.18 eV. The barrier is located "early" on the reaction path for dissociative adsorption, or "late" on the reaction path for associative desorption.

The 2D ground-state potential supports vibrational states. The lowest of these can be classified according to the number of nodes along r and Z. There are 32 bound vibrational levels for 2H:Ru(0001) and 64 for 2D:Ru(0001). The calculated vibrational energies [22] are $\hbar\omega_r = 94$ meV ($758\,\text{cm}^{-1}$) for the r-, and $\hbar\omega_Z = 136$ meV ($1097\,\text{cm}^{-1}$) for the Z-mode. The corresponding experimental values [63] are $\hbar\omega_r = 85$ meV and $\hbar\omega_Z = 140$ meV at a coverage of (1×1). For 2D:Ru(0001), theory gives $\hbar\omega_r = 67$ meV and $\hbar\omega_Z = 97$ meV.

17.3.2.2 The Excited-State Potential and Electronic Lifetime

In the excitation–de-excitation models, relevant excited state potentials are needed. For 2H:Ru(0001) we adopt a single excited state potential $V_a(r, Z)$ with an associated excited-state lifetime, τ_{el}. Reliable *ab initio* calculations of (adsorbate) excited states at

metal surfaces and lifetimes are not yet available. Recently, attempts have been made to calculate excited states of metal/adsorbate systems using cluster approaches in combination with time-dependent DFT (TD-DFT) [64]. Calculations using clusters H_2Ru_n give already with $n = 3$ a multitude of excited states [22]. Most of these have a topology very similar to the ground-state surface. Several of them, however, contain a minimum simultaneously shifted along the r and Z modes by an amount Δ approximately according to

$$V_a(r, Z) = V_g(r - \Delta, Z + \Delta) + E_{ex}. \tag{17.30}$$

All calculations below are for a "representative excited state," with $\Delta = 0.2$ Å. The electronic excitation energy, $E_{ex} = 1.55$ eV, is chosen to match the excitation energy in the experiments.

The excited-state lifetime τ_{el} was varied between 1 and about 10 fs, and thus treated as an empirical parameter. All calculations below refer to $\tau_{el} = 2$ fs. The dependence of the results on different choices for τ_{el} and the potential shift parameter Δ was discussed in Refs [21, 22].

17.3.2.3 Frictional Surfaces and Vibrational Relaxation

In the Langevin model, excited states are not explicitly included but enter the formalism indirectly through the friction coefficients $\eta_{qq'}(r, Z)$ (with $q, q' = r, Z$). Below, we neglect the off-diagonal terms η_{rZ} such that the Langevin equations in the 2D model are

$$m_r \ddot{r} = -\frac{\partial V_g(r, Z)}{\partial r} - \eta_{rr} \dot{r} + R_r(t), \tag{17.31}$$

$$m_Z \ddot{Z} = -\frac{\partial V_g(r, Z)}{\partial Z} - \eta_{ZZ} \dot{Z} + R_Z(t). \tag{17.32}$$

Thus, mode coupling enters only through the potential term. In the equations above, m_r and m_Z are the reduced masses for motion along r and Z, respectively, for 2H:Ru(0001) given as $m_r = m_H/2$ and $m_Z = 2m_H$, respectively (m_H is the hydrogen mass).

The friction coefficients were represented by analytical forms for $\eta_{ZZ}(r, Z)$ and $\eta_{rr}(r, Z)$, which are based on generic models [65] with input from the DFT study on 2H: Ru(0001) of Ref. [20]. These functions are shown in Figure 17.5 along a minimum energy path of the ground-state potential $V_g(r, Z)$, which connects the potential minimum at (r_0, Z_0) with a point corresponding to desorbed H_2 (see also the dotted line in Figure 14.4(a)). The functional forms and parameters are given in the figure caption. From the figure, we note that around the equilibrium position (r_0, Z_0) both coefficients are similar and finite, and both of them vanish when the molecule is away from the surface and cannot couple to the metal electron–hole pairs any more. In between, in particular the η_{ZZ} values vary significantly with the position of the adsorbate relative to the surface.

The frictional terms give rise to vibrational relaxation in the ground electronic state due to vibration-electron coupling. This is demonstrated in Figure 17.6, where the
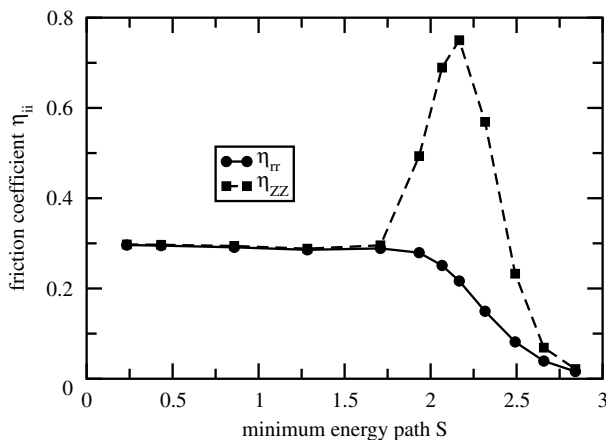
Figure 17.5 Electronic friction coefficients η_{ii} in units of meV ps Å^{-2} along the minimum energy path (S), given in units of Å. $S = 0$ Å corresponds to hydrogen adsorbed at Ru(0001) in the equilibrium position (r_0, Z_0); $S = 2.1$ Å is the transition state and $S = 3$ Å corresponds to the situation where the molecule is about to leave the Ru surface. The functional forms are $\eta_{rr}(r, Z) = a_2 \frac{1}{1 + e^{c(Z - Z_2)}}$ $+ b_2 \exp\left[\frac{-(r - r_2)^2}{2\sigma_r^2} - \frac{(Z - Z_2)^2}{2\sigma_Z^2}\right]$ and $\eta_{ZZ}(r, Z) = a_1 \frac{1}{1 + e^{c(Z - Z_1)}} + b_1 \exp\left[\frac{-(r - r_1)^2}{2\sigma_Z^2} - \frac{(Z - Z_1)^2}{2\sigma_Z^2}\right]$ with the following parameters: $a_1 = a_2 = 0.3$ meV ps Å^{-2}, $b_1 = 0.6$ meV ps Å^{-2}, $b_2 = 0.1$ meV ps Å^{-2}, $c = 4$ Å^{-1}, $Z_1 = 2.36$ Å, $Z_2 = 2.25$ Å, $r_1 = r_2 = 0.74$ Å, $\sigma_Z = 0.2$ Å, $\sigma_r = 0.2$ Å [22].

energy loss (upper panels) and the coordinates r and Z (lower panels) for 2H:Ru (0001) are shown, both as a function of time, for the cases when either the r mode (a) or the Z mode vibration (b) was excited initially. Specifically, single trajectories were run using Eqs. (17.31) and (17.32), with the initial conditions that kinetic energies of $\hbar\omega_r = 94$ meV or $\hbar\omega_Z = 136$ meV were deposited in the respective modes r (a) and Z (b). The initial positions were chosen as the equilibrium values of $r_0 = 2.75$ Å and $Z_0 = 1.06$ Å, respectively. Furthermore, the choice $T_{el} = 0$ K was made. This is equivalent to the assumption that only the r- or Z-excited systems can relax and that electronic re-excitation is impossible because the fluctuating forces vanish. The equations of motion were solved with the help of an algorithm due to Ermak and Buckholz [66].

From an exponential fit of the energies such as

$$E_{tot}(t) = E_{tot}^q(0)\, e^{-t/\tau_{vib}^q}, \tag{17.33}$$

vibrational lifetimes can be estimated for the r and Z modes ($q = r$ and $q = Z$), with $E_{tot}^q(0) = \hbar\omega_q$. Figure 17.6 shows that the exponential form holds well, particularly for the Z mode. One obtains $\tau_{vib}^r = 215$ fs and $\tau_{vib}^Z = 685$ fs. The vibrational relaxation is accompanied by damped oscillations around the equilibrium values r_0 and Z_0.
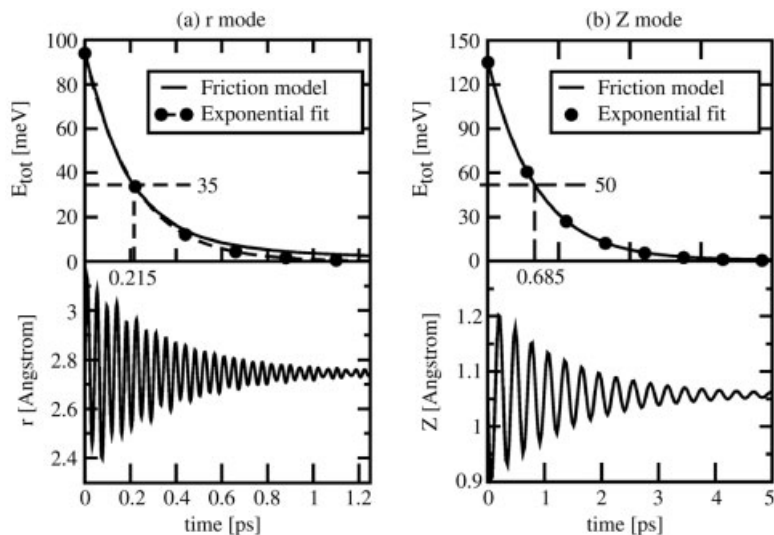
Figure 17.6 The vibrational relaxation of the r (a) and Z mode (b) for 2H:Ru(0001) is shown. Upper panels: The total energy of the system, E_{tot}, as a function of time. From an exponential fit to the data, the vibrational lifetime τ_{vib} can be estimated for each mode as the time when the energy has dropped to $1/e$th of its initial value, $E_{tot}(0)$. Lower panel: The position expectation value along r or Z as a function of time, showing damped oscillations around the equilibrium positions.

17.3.3
DIMET at a Single Laser Fluence

17.3.3.1 Langevin Dynamics Approach

To treat DIMET of H_2 or D_2 for H/D:Ru(0001), the 2D Langevin equations were propagated for many stochastic trajectories. All the trajectories are initialized on the ground-state surface at the adsorption minimum (r_0, Z_0). Initial velocities are chosen from a Boltzmann distribution with a kinetic energy in each mode of $k_B T_{surf}$, with the surface temperature $T_{surf} = 100$ K chosen in accordance with experiment [19]. The trajectories were propagated for 1 ps to equilibrate the system at this temperature. After the initial thermalization period, a visible laser pulse is applied, which heats the metal electrons and the lattice according to the 2TM. The visible pulse was chosen to have the form of a Gaussian temporal shape with 800 nm wavelength and 130 fs FWHM.

When the laser pulse has a fluence of 120 J/m^2, it leads to the electronic temperature as shown in Figure 17.1a, dashed curve. At finite electron temperature, the fluctuating forces R_r and R_Z are different from zero, and the adsorbed H atoms have a chance to associate and desorb as H_2. This is demonstrated in Figure 17.7, where a "representative trajectory" that leads to desorption is shown.
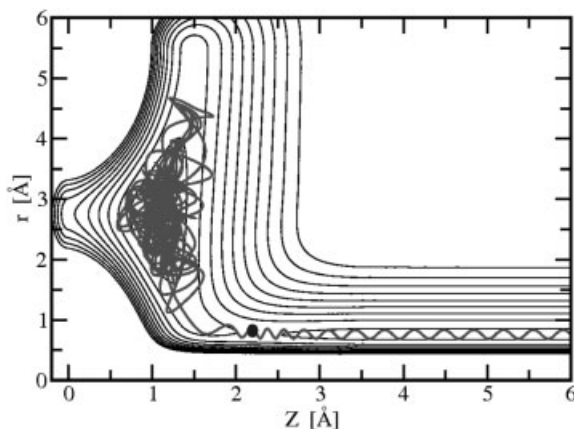
Figure 17.7 An example for a typical trajectory desorbing as molecular hydrogen is overlaid on the ground state PES. The laser fluence was 120 J/m^2. The transition state for associative desorption is indicated by a bullet.

To compare to experiments, one has to do statistics by counting and analyzing the desorbing trajectories for an ensemble of propagations. A trajectory is classified as desorbed, when it is beyond a certain line Z_{des} far from the surface at the end of the propagation time (here, $Z_{des} = 9.5$ Å). Typically, several ten thousands of trajectories are required for desorption of H$_2$ or D$_2$ from Ru(0001). When using $N = 60\,000$ for H$_2$ and $N = 80\,000$ for D$_2$, one obtains a desorption yield of $Y = 2.55 \times 10^{-2}$ for H$_2$ and $Y = 5.46 \times 10^{-3}$ for D$_2$. The desorption probability was calculated as $Y = N_d/N$, where N_d is the number of desorbing trajectories. The yields are *desorption probabilities per laser pulse*, and not very high. Relatively low reaction yields are typical for FL-induced processes at metal surfaces, because quenching and/or electronic friction is very efficient. Various strategies have been suggested how to enhance reactive cross sections, also for metal surfaces [23] – a topic that we will not discuss in this chapter. The larger desorption yield for H$_2$ compared to D$_2$ is consistent with experimental observations [18], and also a consequence of the low desorption yields [23]. Most of the desorptions take place immediately after the peaking of the electronic temperature T_{el} [22], when the fluctuating forces are still large but vibrational relaxation was not yet efficient.

One can also determine average translational and vibrational energies of the desorbing hydrogen molecules. The translational energies are 363 and 324 meV for H$_2$ and D$_2$ with a vibrational energy of 218 and 163 meV, respectively. This unequal energy partitioning is in good agreement with experimental results. The propensity for translation is due to the "late" barrier along the desorption path. It favors translationally rather than vibrationally excited species according to Polanyi's rules. In fact, associative desorption is the reverse reaction to dissociative adsorption. In the latter, translational rather than vibrational energy helps to overcome "early barriers" [67]. The desorption characteristics for H$_2$ and D$_2$ at $F = 120$ J/m^2 according to the Langevin model is summarized in Table 17.1, left half.

Table 17.1 DIMET with 800 nm, 130 fs laser pulses.

|	**Langevin, $F = 120$ J/m²**				**MCWP, $F = 100$ J/m²**		
	Y	E_{trans} (meV)	E_{vib} (meV)		Y	E_{trans} (meV)	E_{vib} (meV)
H₂	2.55×10^{-2}	363	218	H₂	3.78×10^{-3}	454	161
D₂	5.46×10^{-3}	324	163	D₂	7.59×10^{-4}	403	146

a) Left half: Langevin dynamics, at a fluence of 120 J/m². Right half: MCWP dynamics, for a fluence of 100 J/m². Y is the desorption yield, E_{trans} and E_{vib} are the average translational and vibrational energies of desorbing H₂ and D₂ molecules.

17.3.3.2 Stochastic Wave Packet Approach

A similar analysis can be carried out by using the Monte Carlo wave packet method to solve the two-state LvN equation (17.21) for DIMET. To do so, we use the same ground-state potential and the same 2TM as in the Langevin dynamics. The excited state was given by Eq. (17.30), and the electronic lifetime chosen as $\tau_{el} = 2$ fs as described earlier. Starting from the ground vibrational state as initial state, and choosing a laser fluence of $F = 100$ J/m² (with otherwise identical laser parameters as above), one needs about 8000 "quantum trajectories" for H₂ and 10 000 for D₂ to converge results to an accuracy of a small percentage [22]. The propagation of the wave packets was done by a split-operator propagator and by representing the wave functions on a two-dimensional grid. The time–energy method was used to analyze the properties of the desorbing molecules [22].

Desorption arises in this model because the nonvanishing excitation rates $\Gamma_{g \to a}^{el}(t)$ enable population to transfer temporarily from the ground state $|g\rangle$ to the excited state $|a\rangle$. Since the latter is displaced from the ground state by the displacement parameter Δ according to Eq. (17.30), the excited wave packet is nonstationary in the excited state. After return to the ground state within an average lifetime τ_{el}, the wave packet continues to move on $V_g(r, Z)$ until a part of the wave packet can reach the asymptotic region with $Z \to \infty$. Multiple excitations are possible with FL pulses, thereby enhancing the chance of desorption.

In Figure 17.8, the excitation probability is shown not to be very large: The averaged excited-state population $\langle P_a \rangle$ does not exceed 1% or so when a 130 fs laser pulse with $F = 100$ J/m² is applied. As a consequence, in this model, the desorption probability is also small as demonstrated in the right half of Table 17.1. In fact, in the MCWP model, the desorption yield is lower than in the Langevin model. However, it is hard to compare both calculations quantitatively. This is so partly because the Langevin approach is classical. Also, a lower fluence was used in the quantum excitation–de-excitation model and, finally, the results depend somewhat on the excited state potential and lifetimes parameters that are not known accurately [22]. On the positive side, both the classical Langevin and the quantum MCWP models agree in the most important findings: (i) The desorption cross sections are small, (ii) a clear isotope effect is found with H₂ desorbing easier than D₂, and (iii) the desorbing particles are
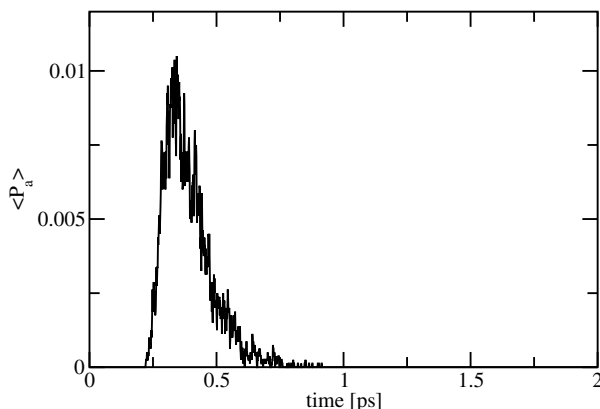
Figure 17.8 Time-dependent electronic excited-state population $\langle P_a \rangle$ for 2H:Ru(0001), for a fluence of 100 J/m^2 in the DIMET model. The populations are averaged over 8000 trajectories obtained from the MCWP method.

much more excited translationally than vibrationally. These similarities are due to the fact that the *desorption process is dominated by the dynamics in the electronic ground state*, even in the excitation–de-excitation models, because the excited-state lifetime is so short [22].

17.3.4
Scaling of DIMET with Laser Fluence

It is therefore also not surprising that both models explain equally well the experimental facts regarding the scaling of desorption yields and other properties of the desorbing molecules with laser fluence. This is demonstrated for H/D:Ru (0001) in Figure 17.9, which shows the desorption yield for H$_2$ and D$_2$ as a function of laser fluence F, and in Figure 17.10, which shows the dependence of energy distributions of the desorbates, also as a function of F [22]. In the classical Langevin case, fluences in the range $\{80, 160\}$ J/m^2 were considered while in the quantum MCWP model we apply fluences within the interval of $\{60, 120\}$ J/m^2. Apart from the different fluence range, the same computational protocols were followed as in Chapter 17.3.3.

From Figure 17.9, it is noted that the desorption yield increases nonlinearly as predicted by Eq. (17.1), both for H$_2$ and D$_2$, and for both models – Langevin (a) and MCWP (b). The computed exponents are somewhat higher than experimentally observed (in particular for MCWP), that is, $n = 2.8$ for H$_2$ and $n = 3.2$ for D$_2$ [18], but still in general agreement. In further agreement with experiment, the isotope ratio $I = Y(H_2)/Y(D_2)$ decreases with increasing F. In the MCWP case, this ratio changes from ~ 10 to 5 in the fluence range $F \in \{60, 120\}$ J/m^2. In the Langevin model, I changes from about 8 to 3 in the range $F \in \{60, 120\}$ J/m^2 [22]. The nonlinear dependence of the desorption probability on fluence is best explained in the MCWP model by the upward rate $\Gamma^{el}_{g \to a}$, which increases dramatically with F as shown in
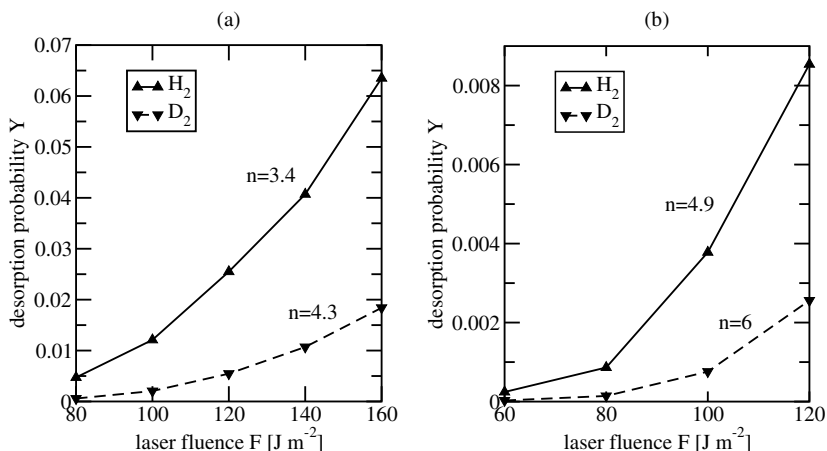
Figure 17.9 Dependence of the desorption yields for H_2 and D_2 on the applied laser fluence calculated with the classical Langevin method (a) and the quantum MCWP case (b). In the former, simulations are performed for $F \in \{60, 120\}$ J/m², and an excited-state lifetime of 2 fs. In the latter, fluences F are taken in the range, $\{80, 160\}$ J/m². All curves are associated with a different value of the power law constant, n according to Eq. (17.1).

Figure 17.1c. As a consequence, increasing the fluence greatly enhances the electronic excitation probability. This can also be seen from the average number of electronic excitations that increase with fluence as quantitatively demonstrated in Ref. [22]. In that study, it is found that at $F = 60$ J/m², the average number of excitation–de-excitation cycles per pulse is 0.13, and that the probability of multiple excitations is vanishingly small. At $F = 120$ J/m², on the other hand, the average
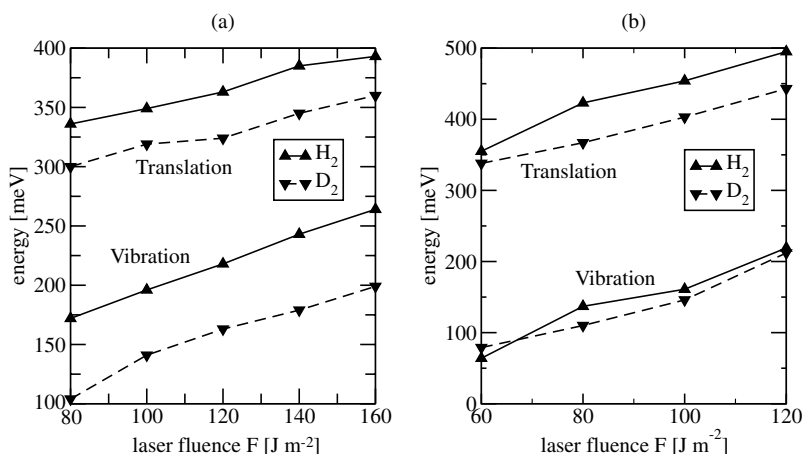
Figure 17.10 (a) Fluence dependence of vibrational and translational energies obtained from the Langevin simulations for different fluences for H_2 and D_2, in the fluence range $F \in \{80, 160\}$ J/m². (b) The same for the quantum MCWP case, and a fluence range of $F \in \{60, 120\}$ J/m².

number of excitation–de-excitation cycles is 1.5, and the probability of multiple excitations is high – up to sixfold excitations were observed in Ref. [22]. As a result, more molecules reach higher vibrational levels on the ground electronic state after the final electronic relaxation when high fluences are used, and this promotes desorption. The process is highly nonlinear, thus resulting in a nonlinear scaling as in Eq. (17.1).

Figure 17.10 illustrates the nearly linear increase with fluence found in the computed translational and vibrational energies. The increasing energy content in the product channels with increasing fluence arises because the latter leads to more energy absorption and hence more energy can be released into the desorbates. The translation remains hotter compared to vibration and H_2 acquires more energy than D_2 in both modes. These two findings are in good agreement with experimental observations [19]. For example, the translational energy of D_2 increases from about 300 to 500 meV in the fluence range $F \in \{60, 120\}$ J/m^2 according to the experiment studied in Ref. [19]. Our corresponding theoretical values are 338 meV (at 60 J/m^2), and 443 meV (at 120 J/m^2), respectively. In further agreement with experiment, the ratio between translational and vibrational energies, E_{tr}/E_{vib}, decreases from 5.6 to 2.3 for H_2 and from 4.3 to 2.1 for D_2, respectively. This is due to the fact that the additional energy gained by the desorbing molecule at higher fluences is approximately equally distributed between translation and vibration, that is, the difference between energies remains nearly constant while their ratio changes.

17.4
Conclusions

Theoretical concepts for the treatment of femtochemistry at solid surfaces can be categorized as effective single-state ("weakly nonadiabatic") or nonadiabatically coupled multistate models ("strongly nonadiabatic"), respectively. At metal surfaces, the electronically excited states that enforce the nuclear motion toward new products are typically very-short lived ($\sim$ fs). As a consequence, the nuclear dynamics proceeds in the electronic ground state for most of the time. This explains why, if the same ground-state potentials are used, semiquantitative agreement is obtained for both sets of theories. The importance of quantum effects in the nuclear coordinates is not quite clear because classical treatments of the nuclear motion is often sufficient to explain the major effects. Note, however, that the explicit inclusion of electronically excited states is, by definition, at least partially quantum in nature. FL-induced dynamics at surfaces, notably at metal surfaces, in practice requires system-bath-type models because coherent, multistate models cannot be realized computationally. In the Langevin approach, the (electron–hole) "bath" enters through friction coefficients, while in the excitation–de-excitation models the excited electronic states are short-lived. For the laser excitation of metal electrons, the concept of a time-dependent electron temperature is useful, but limitations are known.

Despite their similarities, both the "weakly nonadiabatic" friction and the "strongly nonadiabatic" excitation–de-excitation models of femtosecond laser chemistry rely

on different assumptions. Therefore, there are also clear differences that may lead to different interpretations of the desorption dynamics [32]. For example, the two- and multistate models account for dynamical details arising from the characteristic topology of the excited state potential, for example, the postexcitation "inward motion" in the Antoniewicz models of photodesorption [4]. In the friction models, the excited states enter only implicitly, for example, through the friction coefficients $\eta_{qq'}$ and their coordinate dependence. Furthermore, in the friction model, vibrational relaxation and desorption are deeply interconnected: Without the former, the latter cannot happen. In contrast, in the excitation–de-excitation models, vibrational relaxation is merely a small correction while electronic relaxation is decisive [32].

These differences are due to different approximations for the underlying physics. Still, both sets of models are capable of describing femtochemistry at surfaces semiquantitatively. It should now be the goal to extend the approaches toward computationally tractable multidimensional simulation tools, and to include hereto neglected effects such as coupling to surface phonons. Ideally, these models should use input only from *first principles* electronic structure theory. It will then be interesting to apply the tools also to other FL-induced elementary processes at adsorbate-covered metal surfaces, such as photodissociation [68], photodiffusion [69, 70], or more complex photoreactions [11].

Acknowledgment

References

1 Ertl, G. (1990) *Angew. Chem. Int. Ed.*, **29**, 1219.

2 Menzel, D. and Gomer, R. (1964) *J. Chem. Phys.*, **41**, 3311.

3 Redhead, P.A. (1980) *Can. J. Phys.*, **42**, 886.

4 Antoniewicz, P.R. (1980) *Phys. Rev. B*, **21**, 3811.

5 Ho, W. (1996) *Surf. Sci.*, **363**, 166.

6 Frischkorn, C. and Wolf, M. (2006) *Chem. Rev.*, **106**, 4207.

7 Vondrak, T. and Zhu, X.-Y. (1999) *Phys. Rev. Lett.*, **82**, 1967.

8 Buntin, S.A., Richter, L.J., Cavanagh, R.R., and King, D.S. (1988) *Phys. Rev. Lett.*, **61**, 1321.

9 Kidd, R.T., Lennon, D., and Meech, S.R. (1999) *J. Phys. Chem. B*, **103**, 7480.

10 Hohlfeld, J., Wellershoff, S.-S., Güdde, J., Conrad, U., Jähnke, V., and Matthias, E. (2000) *Chem. Phys.*, **251**, 237.

11 Bonn, M., Funk, S., Hess, Ch., Denzler, D.N., Stampfl, C., Scheffler, M., Wolf, M., and Ertl, G. (1999) *Science*, **285**, 1042.

12 Denzler, D.N., Frischkorn, C., Hess, C., Wolf, M., and Ertl, G. (2003) *Phys. Rev. Lett.*, **91**, 226102.

13 Morin, M., Levinos, N.J., and Harris, A.L. (1992) *J. Chem. Phys.*, **96**, 3950.

14 Prybyla, J.A., Heinz, T.F., Misewich, J.A., Loy, M.M.T., and Glownia, J.H. (1990) *Phys. Rev. Lett.*, **64**, 1537.

15 Misewich, J.A., Heinz, T.F., and Newns, D.M. (1992) *Phys. Rev. Lett.*, **68**, 3737.

16 Budde, F., Heinz, T.F., Loy, M.M.T., Misewich, J.A., deRougemont, F., and Zacharias, H. (1991) *Phys. Rev. Lett.*, **66**, 3024.

17 Budde, F., Heinz, T.F., Kalamarides, A., Loy, M.M.T., and Misewich, J.A. (1993) *Surf. Sci.*, **283**, 143.

18 Denzler, D.N., Frischkorn, C., Wolf, M., and Ertl, G. (2004) *J. Phys. Chem. B*, **108**, 14503.

19 Wagner, S., Frischkorn, Ch., Wolf, M., Rutkowski, M., Zacharias, H., and Luntz, A. (2005) *Phys. Rev. B*, **72**, 205404.

20 Luntz, A.C., Persson, M., Wagner, S., Frischkorn, C., and Wolf, M. (2006) *J. Chem. Phys.*, **124**, 244702.

21 Vazhappilly, T., Beyvers, S., Klamroth, T., Luppi, M., and Saalfrank, P. (2007) *Chem. Phys.*, **338**, 299.

22 Vazhappilly, T., Klamroth, T., Saalfrank, P., and Hernandez, R. (2009) *J. Phys. Chem. C*, **113**, 7790.

23 Saalfrank, P. (2006) *Chem. Rev.*, **106**, 4116.

24 Kaganov, M.I., Lifshitz, I.M., and Tanatarov, L.V. (1957) *Sov. Phys. JETP*, **4**, 173.

25 Anisimov, S.I., Kapeliovich, B.L., and Perel'man, T.L. (1974) *Zh. Eksp. Teor. Fiz.*, **66**, 776.

26 Corkum, P.B., Brunel, F., Sherman, N.K., and Srinivasan-Rao, T. (1988) *Phys. Rev. Lett.*, **61**, 2886.

27 Nest, M. and Saalfrank, P. (2004) *Phys. Rev. B*, **69**, 235405.

28 Brandbyge, M., Hedegård, P., Heinz, T.F., Misewich, J.A., and Newns, D.M. (1995) *Phys. Rev. B*, **52**, 6042.

29 Fann, W.S., Storz, R., Tom, H.W.K., and Bokor, J. (1992) *Phys. Rev. Lett.*, **68**, 2834.

30 Weik, F., de Meijere, A., and Hasselbrink, E. (1993) *J. Chem. Phys.*, **99**, 682.

31 Knorren, R., Bouzerar, G., and Bennemann, K.-H. (2001) *Phys. Rev. B*, **63**, 094306.

32 Nest, M. and Saalfrank, P. (2002) *J. Chem. Phys.*, **116**, 7189.

33 Gao, S., Lundquist, B.I., and Ho, W. (1995) *Surf. Sci.*, **341**, L1031.

34 Tully, J.C., Gomez, M., and Head-Gordon, M. (1993) *J. Vac. Sci. Technol. A*, **11**, 1914.

35 Press, W.H., Teukolsky, S.A., Vetterling, W.T., and Flannery, B.P. (2003) *Numerical Recipes*, 2nd edn, Cambridge University Press, Cambridge.

36 Luntz, A.C. and Persson, M. (2005) *J. Chem. Phys.*, **123**, 074704.

37 Gao, S. (1997) *Phys. Rev. B*, **55**, 1876.

38 Anderson, P.W. (1961) *Phys. Rev.*, **124**, 41.

39 Newns, D.M. (1969) *Phys. Rev.*, **178**, 1123.

40 Saalfrank, P., Baer, R., and Kosloff, R. (1994) *Chem. Phys. Lett.*, **230**, 463.

41 Saalfrank, P. and Kosloff, R. (1996) *J. Chem. Phys.*, **105**, 2441.

42 Zoller, P., Marte, M., and Walls, D.F. (1987) *Phys. Rev. A*, **35**, 198.

43 Dum, R., Zoller, P., and Ritsch, H. (1992) *Phys. Rev. A*, **45**, 4879.

44 Dalibard, J., Castin, Y., and Mølmer, K. (1992) *Phys. Rev. Lett.*, **68**, 580.

45 Mølmer, K., Castin, Y., and Dalibard, J. (1993) *J. Opt. Soc. Am. B*, **10**, 524.

46 Saalfrank, P. (1996) *Chem. Phys.*, **211**, 265.

47 Saalfrank, P., Boendgen, G., Finger, K., and Pesce, L. (2000) *Chem. Phys.*, **251**, 51.

48 Gao, S., Strömquist, J., and Lundqvist, B.I. (2001) *Phys. Rev. Lett.*, **86**, 1805.

49 Guo, H. (1997) *J. Chem. Phys.*, **106**, 1967.

50 Tully, J.C. (1990) *J. Chem. Phys.*, **93**, 1061.

51 Blais, N.C. and Truhlar, D.G. (1983) *J. Chem. Phys.*, **79**, 1334.

52 Coker, D.F. and Xiao, L. (1995) *J. Chem. Phys.*, **102**, 496.

53 Krylov, A.I., Gerber, R.B., and Coalson, R.D. (1996) *J. Chem. Phys.*, **105**, 4626.

54 Müller, U. and Stock, G. (1997) *J. Chem. Phys.*, **107**, 6230.

55 Groß, A. and Bach, C. (2001) *J. Chem. Phys.*, **114**, 6396.

56 Carbagno, C., Groß, A., and Rohlfing, M. (2007) *Appl. Phys. A*, **88**, 579.

57 Luppi, M., Oslen, R.A., and Baerends, E.J. (2006) *Phys. Chem. Chem. Phys.*, **8**, 688.

58 Vincent, J.K., Olsen, R.A., Kroes, G.-J., Luppi, M., and Baerends, E.-J. (2005) *J. Chem. Phys.*, **122**, 044701.

59 DACAPO code, http://www.fysik.dtu.dk/campos/Dacapo.

60 Hammer, B., Hansen, L.B., and Nørskov, J.K. (1999) *Phys. Rev. B*, **59**, 7413.

61 Busnengo, H.F., Salin, A., and Dong, W. (2000) *J. Chem. Phys.*, **112**, 7641.

62 Vincent, J.K., Olsen, R.A., Kroes, G.-J., Luppi, M., and Baerends, E.-J. (2005) *J. Chem. Phys.*, **122**, 044701.

63 Shi, H. and Jacobi, K. (1994) *Surf. Sci.*, **313**, 289.

64 Besley, N.A. (2004) *Chem. Phys. Lett.*, **390**, 124.

65 Diekhöner, L., Hornekær, L., Mortensen, H., Jensen, E., Baurichter, A., Petrunin, V.V., and Luntz, A.C. (2002) *J. Chem. Phys.*, **117**, 5018.

66 Allen, M.P. and Tildesley, D.J. (1987) *Computer Simulation of Liquids*, Oxford University Press, New York.

67 Halstead, D. and Holloway, S. (1990) *J. Chem. Phys.*, **93**, 2859.

68 Camillone, N. III, Khan, K.A., Lasky, P.J., Wu, L., Moryl, J.E., and Osgood, R.M. Jr. (1998) *J. Chem. Phys.*, **109**, 8045.

69 Bartels, L., Wang, F., Möller, D., Knoesel, E., and Heinz, T.F. (2004) *Science*, **305**, 648.

70 Stépán, K., Güdde, J., and Höfer, U. (2005) *Phys. Rev. Lett.*, **94**, 236103.